APPLIED SCIENCES AND ENGINEERING

Automated design of 3D DNA origami with non-rasterized 2D curvature

Daniel Fu[1]†, Raghu Pradeep Narayanan[2]†, Abhay Prasad[3]†, Fei Zhang[4], Dewight Williams[5], John S. Schreck[6], Hao Yan[3]*, John Reif[1]*

Improving the precision and function of encapsulating three-dimensional (3D) DNA nanostructures via curved geometries could have transformative impacts on areas such as molecular transport, drug delivery, and nanofabrication. However, the addition of non-rasterized curvature escalates design complexity without algorithmic regularity, and these challenges have limited the ad hoc development and usage of previously unknown shapes. In this work, we develop and automate the application of a set of previously unknown design principles that now includes a multilayer design for closed and curved DNA nanostructures to resolve past obstacles in shape selection, yield, mechanical rigidity, and accessibility. We design, analyze, and experimentally demonstrate a set of diverse 3D curved nanoarchitectures, showing planar asymmetry and examining partial multilayer designs. Our automated design tool implements a combined algorithmic and numerical approximation strategy for scaffold routing and crossover placement, which may enable wider applications of general DNA nanostructure design for nonregular or oblique shapes.

INTRODUCTION

DNA origami (*1*) is an enticing technique for nanoscale design because of its simple and consistent design principles (*2–7*), from which it can produce self-assembling (*8–14*), spatially organized nanomaterials (*15–17*) to study nanoscale phenomena (*18–31*). The catalog of DNA origami shapes and their respective underlying design strategies has become increasingly varied by exploitation of algorithmic principles and optimization of synthesis conditions (*32–36*). Many three-dimensional (3D) DNA origami shapes can also be designed in such a way as to serve as a separating barrier between encapsulated internal moieties and an external environment. Emerging applications using encapsulating 3D DNA nanostructures have affected areas such as nanoparticle synthesis (*37, 38*), low-volume reactors (*39, 40*), templated assembly (*41–43*), molecular transport (*44–48*), or drug delivery (*49–53*). These applications often demand rigid, hollowed structures or, in other words, capsule-like functionality. Thus far, DNA nanostructures tailored toward interdisciplinary applications remain constrained to a relatively limited variety of forms; most are still based on designs arising from strategies that are founded upon a traditional strategy where helices are straight and parallel to a common vector (*2*).

Earlier work proposed a contrasting strategy based on curved DNA helices, which were better suited for developing a wide variety of capsule-like structures (*3, 4*). Curvature can provide a finer-grained discretization of addressable locations and geometries (*31, 38, 42*) and create enclosed shapes with larger compartments more economically than block-based designs (*39, 52*). Curved motifs also align more closely with naturally occurring or globular molecules (*43*) while still maintaining an enclosed space that is suitable for consolidating molecular activity.

However, while the benefits of novel DNA nanostructures that are stable, curved, and fully enclosed and that achieve practical yields are evident, the high complexity of designing these structures has hindered its accessibility to researchers. Furthermore, current design principles for enclosed, curved DNA nanostructures have mostly been demonstrated for single-layer nanostructures, which limit the achievable rigidity and applications. This work expands the design space of enclosed, curved DNA nanostructures and introduces the DNAxiS [Computer-aided design (CAD)] for DNA nanostructures with axial symmetry) software tool to automate the corresponding escalation in design tedium. We introduce -previously unknown, multilayer design strategies (*33–36*) specifically for curved DNA nanostructures under the term reinforcement, which leads to increasing the overall yield and stability by only targeted application of multilayer design principles to segments in the structure. DNAxiS is the first CAD software tool implementing probabilistic algorithms to perform crossover selection and the first for the design of capsule-like curved DNA nanostructures, with a specific focus on those with axial symmetry (DNAxiS is standalone, open-source software with more information and an online version available at http://caddna.cs.duke.edu).

RESULTS

Design principles of curved, enclosed DNA origami nanostructures

DNA origami nanostructures are typically synthesized by annealing in one-pot reactions using a large set of short oligonucleotides [<100 base pairs (bp)] called staples to "fold" a long (>1000 bp) single-stranded DNA strand termed the scaffold into a desired physical conformation (*1*). Subsequences of a staple strand bind to corresponding complementary sequences upon the scaffold

[1]Department of Computer Science, Duke University, Durham, NC, USA. [2]Department of Cellular and Molecular Pharmacology, University of California, San Francisco, San Francisco, CA, USA. [3]School of Molecular Sciences and Center for Molecular Design and Biomimetics at Biodesign Institute, Arizona State University, Tempe, AZ, USA. [4]Department of Chemistry, Rutgers University, Newark, NJ, USA. [5]Erying Materials Center, Office of Knowledge Enterprise Development, Arizona State University, Tempe, AZ, USA. [6]National Center for Atmospheric Research (NCAR), Computational and Information Systems Laboratory, Boulder, CO, USA.
*Corresponding author. Email: hao.yan@asu.edu (H.Y.); reif@cs.duke.edu (J.R.)
†These authors contributed equally to this work.

strand, and where a continuous staple sequence binds between discontinuous sequences on the scaffold will generate a crossover on the staple DNA to link the two discontinuous domains of the scaffold. Therefore, the particular placement and distribution of crossovers across the entire sequence (we refer to as the crossover network) play an important role in maintaining the overall shape, stability, and rigidity of the resultant nanostructure by balancing and distributing strain.

Curved DNA origami nanostructures are created by applying those fundamental techniques to a template based on arranging helices as circles. Each circular helix, or ring, and its adjacent rings have varying z axis placement and circumference, thus forming rounded, extruded structures with non-rasterized curvature within the xy plane. The full, enclosed geometry is designed by calculating circumferences of adjacent pairs of rings to reduce gaps down to the interhelical distance ($\delta = 2.6$ nm). Furthermore, circumferences are rounded to make an integer number of DNA full turns and to the closest multiple of a crossover factor, choosing one of 3, 4, or 5 consistently for the entire structure; the chosen value is a common divisor of the number of crossovers that are formed between each pair of nearest neighbor rings and, by doing so, promotes symmetry and regularity in the design. When rings are planar, this corresponds to 48 or 50 bp.

Because of these differences in circumference throughout the structure, the nominal twist of B-form DNA cannot always be persistently preserved. As specified by previous work (4), placing crossovers such that all sections of the DNA helices are between 9 and 12 bp per turn will help to maintain a high yield of the intended structure. Furthermore, the crossover network is interspersed such that adjacent crossovers are not set too close, which can concentrate strain upon that segment of the structure and lower yield, or not too far, which may not provide enough strain to maintain curvature against the persistence length of DNA. This corresponds roughly to a crossover spacing of two to five full turns of DNA between
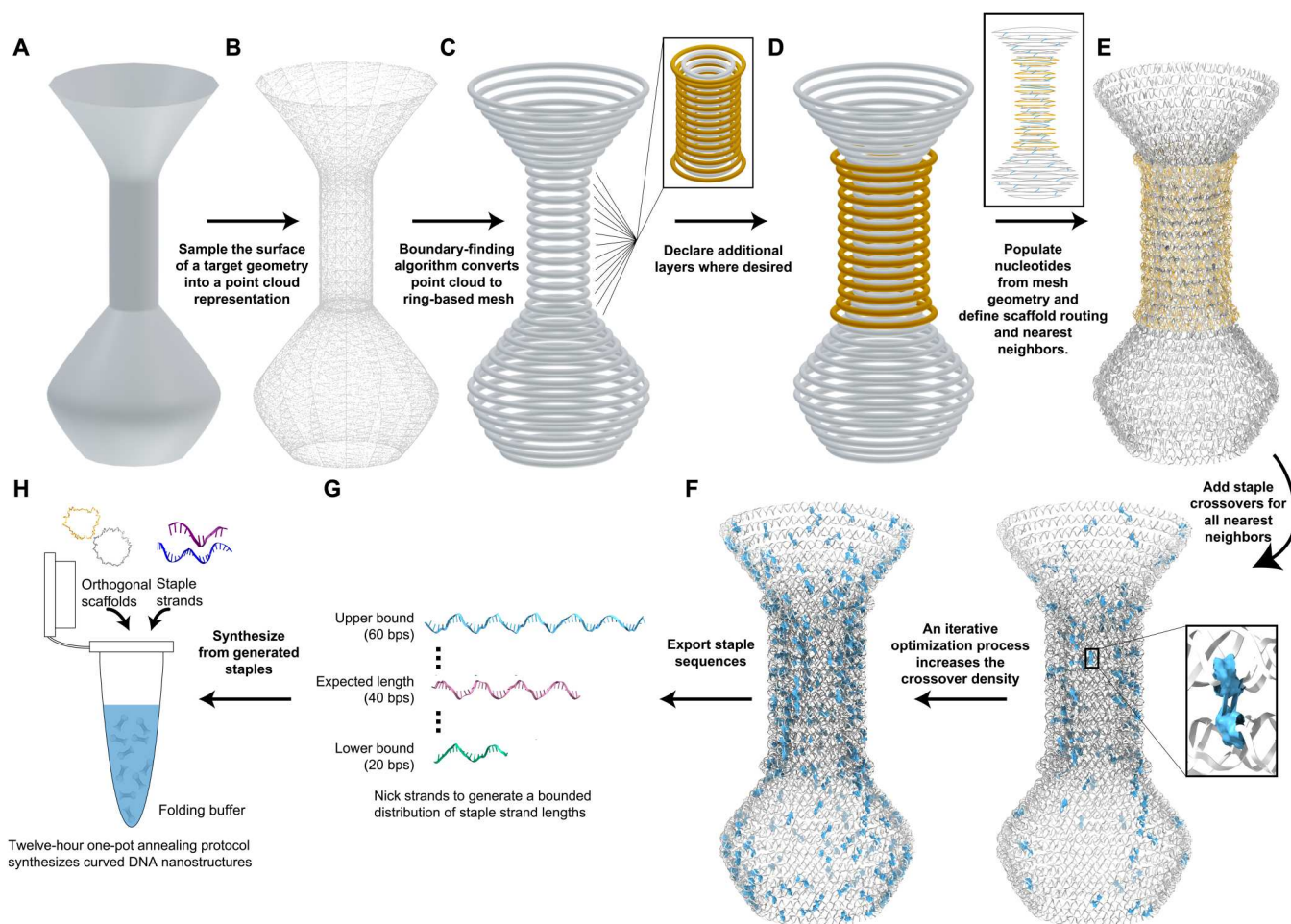

Fig. 1. Overview of the DNAxiS design process. (**A**) User input is a 3D model in STL file format generated in the user's graphics design software of choice. (**B**) The vertices of the STL build a point cloud that is upsampled to avoid gaps when extracting the shape's outline (fig S1). (**C**) A circle-based mesh is extracted from the point cloud. (**D**) The structure can be made selectively multilayer by adding rings outward from the starting mesh. (**E**) A helical twist is calculated from the circumference and used to convert each circle of the mesh into a DNA helix ring. (**F**) Crossovers are densely applied upon the template using either a greedy algorithm or a simulated annealing algorithm. (**G**) Conventional scaffold sequences are applied to generated corresponding staple sequences within specified length bounds. (**H**) Staple sequences are annealed with the corresponding scaffolds, sometimes multiple orthogonal sequences as needed, in a one-pot reaction to produce DNA nanostructures of the designed shape.

adjacent crossovers spanning the same pair of helices. (Example circumferences resulting from variations in these parameters are shown in table S1.)

Moreover, creating curvature on such short double helices will naturally result in a higher strained conformation of double-stranded DNA, which can cause a higher number of staples to bind incorrectly, thus lowering the overall yield of properly formed DNA nanostructures. This is more strongly expressed in curved nanostructures because of the presence of each staple being more crucial for preserving local curvature. Multilayer designs not only provide redundancy in staple density to overcome binding errors but are also expected to be more mechanically rigid (33, 34), while careful design choices and synthesis conditions can further promote the formation of well-formed structures.

Overview of DNAxiS software and challenges to curved DNA nanostructure design

DNAxiS is the first software tool to implement a general algorithm for designing curved DNA nanostructures respecting the above constraints while extending the design space to accommodate multilayer designs. The lattice-free nature of helix placement and crossover placement of curved DNA origami design distinguishes it from the capabilities of previous design algorithms and interfaces (6, 7, 32, 54–56). The design of multilayer, curved nanostructures face unique challenges primarily emerging from the presence of continuous, curved helices, as opposed to straight or disjointed helices. Without a strong basis for algorithmic regularity or crossover periodicity arising from straight helices, DNAxiS instead applies heuristic algorithms that closely mimic concepts and approaches applied by a human designer when routing a scaffold strand or distributing a crossover network in DNA origami nanostructures.

The overall internal processing procedure of DNAxiS is illustrated in Fig. 1, and an overview of the crossover placement algorithms is described later. In summary, the process begins by specifying a shape via a standard triangle language (STL) file externally designed in the user's 3D design software of choice (e.g., SolidWorks, Fusion 360, Blender, etc.) (Fig. 1A). The model is processed to extract a shape that is discretized into a ring-based mesh (Fig. 1, B and C, and fig. S1), where each ring represents the placement of a circular DNA helix. Additional rings can be manually placed, which can be used to indicate an expansion of the mesh to a multilayer design. The user also helps to define the scaffold routing and nearest neighbors (Fig. 1D and fig. S2). The total mesh, replaced by DNA helices (Fig. 1E), is referred to as the template. The template specifies the position of each helix and its nucleotides in a coordinate space. The crossover placement algorithms are then applied upon the template to connect the helices together via crossovers (Fig. 1F), finally determining a dense-enough crossover network that can be exported toward synthesis (Fig. 1, G and H).

A major challenge for moving into a curved design space is that crossover positions no longer appear with a small periodicity in curved DNA nanostructures as they do with straight helices, appearing once every several turns instead of once every one turn (fig. S4). Some existing methods of 3D DNA origami design form encapsulating nanostructures using rectilinear designs (2, 37–40). Others can estimate curvature by cyclically linking short, straight sections
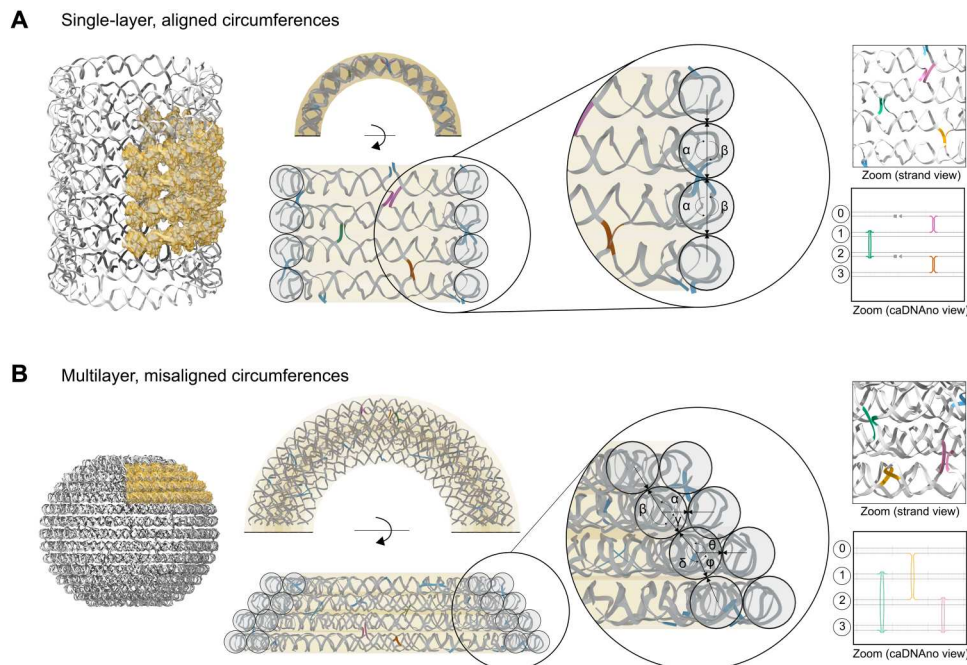

Fig. 2. Alignment principles for single/multilayer, curved, closed-shell DNA nanostructures. (**A**) As a single-layer structure without varying circumferences, the crossover network of a cylinder is no more complex than a flat DNA origami rectangle. Local patterns of a few crossovers can be repeated globally, as the dihedral angle and crossover periodicity are the same for all pairs of nearest neighbor helices. (**B**) Extension of design principles to multilayer, curved, and closed-shell DNA nanostructures significantly complicates the design space for determining valid crossovers. Each crossover pattern between pairs of nearest neighbor helices is unique because of a different dihedral angle and varying helical twists. Rather than repeating a simple local pattern, each crossover, typically up to 200 when fully using a single M13mp18 scaffold, must be carefully positioned. DNA origami nanostructres were designed using caDNAno software. DNA origami nanostructures were designed using caDNAno software."

by single-stranded corners (*56*). The straight edges in these design methodologies do not have problems with low crossover periodicity, but this can either introduce gaps or undersample the desired curvature. The irregular circumference of curved DNA nanostructures also obfuscates crossover positions, especially to a human designer. Curvature in the most basic curved structures, such as a cylinder, can still exploit the global repetition of local crossover patterns in a similar fashion to DNA origami based on straight, antiparallel helices. As shown in Fig. 2, a shift to multilayer, curved structures from single-layer, vertically aligned patterns expand the problem space as each pair of adjacent helices may require a unique crossover pattern. This is the most substantial departure from previous DNA design strategies and their automations. Furthermore, these irregularities often force a designer to choose nonideal crossover positions, which additionally contribute strain into the structure. Considering crossovers in a rated and ranked order can offset damaging overselection of crossovers that have high contributions of global strain. This problem is also more prevalent in multilayer structures, where each helix connects to more nearest neighbors and further complicates the placement of adjacent crossovers within a single helix due to reducing the average spacing between adjacent crossovers. Lower spacing shortens the length of continuous regions of complementary staple to scaffold sequences. Then, weaker binding of each staple strand reduces yields.

Crossover network heuristic optimization algorithms

Several constraints are active in determining valid crossover positions to fully determine a crossover network for forming the nanostructure. Potential crossover positions between a pair of helices are first determined by looking for collinearity of a bisecting vector through the dihedral angles between any pair of adjacent nucleotides (fig. S3). Then, all pairwise combinations of crossover positions are evaluated for their alignment, which is the expected distance that a backbone bond between crossover nucleotides must overcome to form the crossover. Impractical crossover positions are eliminated above a threshold for their alignment, indicating that the two points on each helix are too far apart. The remaining set of crossover positions is then ranked by alignment. Worse alignments are believed to lead to worse yields, although this has not been fully quantified. Second, crossovers are ranked by their base pair distance from another crossover. The leading crossover of this list is then popped and applied in an order depending on two separately implemented algorithms for crossover placement.

The initial strategy of completing the crossover network implements a unique algorithm (fig. S5) that makes a single pass through the nanostructure and leads to localized improvements. In this strategy, crossovers between each pair of helices are an independent problem. Between each pair of adjacent helices, the algorithm aims to create a fixed number of crossovers by always accepting the best-ranked crossover, updating that list, and repeating this process. Upon failure, the accepted threshold of crossover alignment is incremented to provide more options and avoid starving a crossover set with overly tight constraints for connecting subsequent pairs of rings. This method can be fast but makes little consideration for global context of each crossover and risks an imbalanced or skewed placement across the entire geometry.

A simulated annealing method can improve upon this strategy by implementing a heuristic optimization algorithm (figs. S6 and

S7) that finds a global optimum through a biased random walk through a series of minutely different conformations of the crossover network. In this augmented strategy, crossovers between pairs of helices are dependent on the solution of their neighboring pairs. Each state is scored by the highest-spaced pair of crossovers, and the goal of the algorithm is to find a crossover network with as low of a score as possible, implying a high and uniform density of crossovers. It begins by initializing a temperature factor T with a high integer value (e.g., $T = 30$). As the state space is traversed, paths are rejected when the score of the new conformation exceeds the score of the current conformation plus the temperature factor. This biases the walk toward finding a global optimum while providing opportunities in the random walk to escape traps of local optima. This method is much slower, taking up hours for large structures (fig S8), but can implement denser, more uniform crossover networks with minimal effort from the user.

Experimental evaluation of curved, enclosed DNA nanostructures with crossover networks generated by heuristic algorithms

A mix of these localized and global heuristic approaches toward freeform design was then verified in simulation and experimental demonstration of some archetypal geometries—bowl, gourd, and sphere—which vary in their inflection between concavity and convexity along different axes, while also differing between sharp or soft inflections. The bowl is hyperbolic with a vertical axis parallel to the axis of rotation. The inflection occurs between helices that have, in order, 10.17, 11.25, and 10.58 bp per turn of helical twist, therefore limiting the number of crossovers that will align on small periods. Its inflection point at the rim of the bowl is approximately 48°, so crossovers to each adjacent helix from their common, middle helix will likely differ by only 1 bp along the helix. Under conventional and stringent constraints, there would be scarce choices for crossovers, but via a relaxation of spacing and alignment criteria, additional valid crossovers are found and applied to form the structure. The gourd is hyperbolic with a vertical axis perpendicular to the axis of rotation. Multiple inflection points demonstrate that there is no issue for the outline of the structure to follow a freeform path. The sphere is designed to be fully multilayer. As opposed to single layer, each helix can potentially have crossovers to three nearest neighbor helices rather than only two. For the larger circumferences within the structure, to maintain crossover spacing and density, as many as 20 crossover positions may need to be found along a single helix to maintain a stable connection with each of its neighbors. Crossover choices from a single helix also propagate to and reduce crossover choices available for an adjacent helix, which creates a decision-making chain that appears intractable for a human designer but can nonetheless be implemented by a series of fairly straightforward queries in computational design.

As DNAxiS also exports to formats compatible with widely used molecular dynamics simulators, such as oxDNA (*57–60*), we were able to prototype designs more economically in silico in conjunction with experimental demonstrations. Figure 3 shows the design and characterization of each archetypal geometry. Mean structures calculated from molecular dynamics simulations indicated that structures were likely to form the intended shape. Thus, we proceeded to test them experimentally, with yields characterized by agarose gel electrophoresis (AGE) and structures observed by transmission electron microscopy (TEM). All shapes formed with good yields
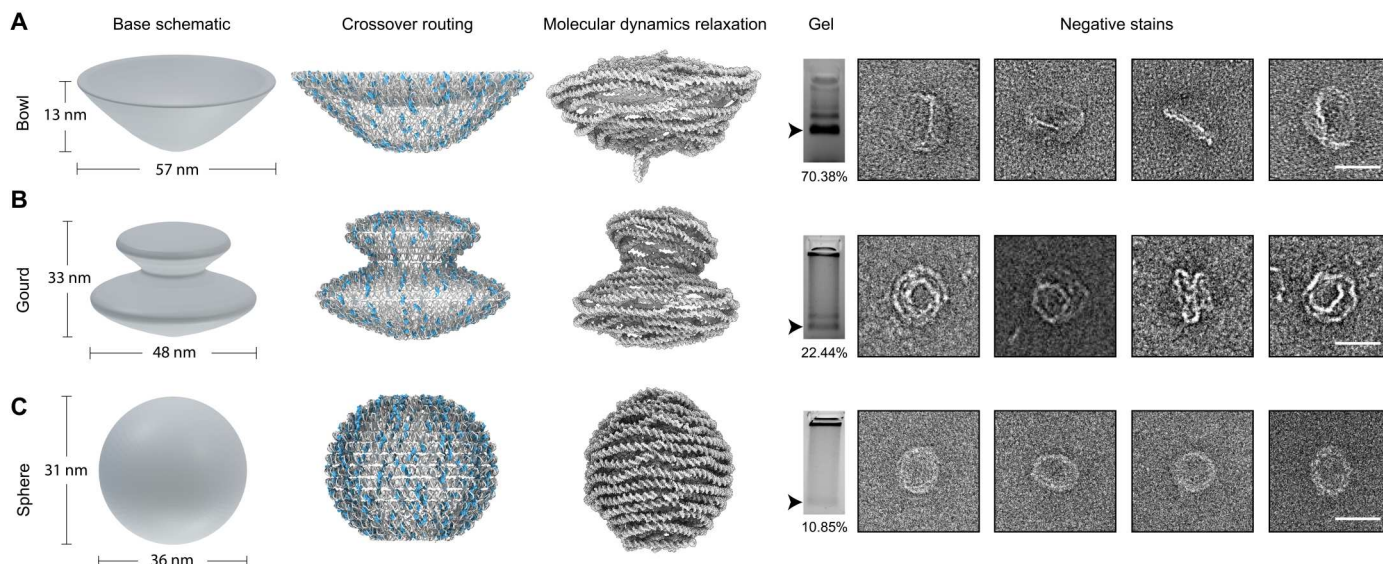
Fig. 3. Experimental verification of automated design principles. (**A**) Bowl design evaluates convex and concave inflection horizontally with respect to its axis of rotation. Scale bar, 40 nm. (**B**) Gourd design evaluates convex and concave inflection vertically along its profile, perpendicular to the axis of rotation. Scale bar, 40 nm. (**C**) Sphere is designed with two layers, one nested and one encapsulating, to evaluate the extension of design principles to multilayer structures. Scale bar, 40 nm.

(bowl = 70.38%, gourd = 22.44%, and sphere = 10.85%) (figs. S9 to S14).

However, while the bowl and gourd formed well, a portion of other single-layer designs that were designed and characterized did not, either with low yields or showing malformed geometries (Fig. 4, D, F, and H, and figs. S15 to S20). We continue by designing multilayer versions of those single-layer designs under similar criteria to the sphere. In particular, we were interested in whether an extension of the automated methods toward multilayer structures could generate structures of the same shape but with higher yield and improved shape accuracy.

Evaluating yield and feature formation in multilayer designs

Thus, the efficacy of reinforcement was tested. Partial multilayer designs are created by the addition of two design principles. First, multilayer sections are defined by adding coplanar helices outward from each helix within a chosen section of the single-layer design (fig. S1). All planes are perpendicular to the shape's axis of rotation. This forms another layer with a similar topology as the single layer. In addition, the path of the scaffold through the helices is fulfilled in plane first, forming a "zig-zag" pattern (fig. S2). This allows anywhere along the structure to be reinforced, instead of only at the top or bottom.

Initially, in oxDNA, we investigated the effects of reinforcement in basic cylinder and sphere shapes for up to three additional layers (fig. S21). However, most likely because of tradeoffs between crossover spacing and density, increases in mechanical rigidity tapered after the addition of only one additional layer. Thus, these same methodologies were then applied using only one additional reinforcing layer, first upon the neck of a vase design (Fig. 4A). In its single-layer variant, the neck conforms less to the intended cylindrical design while also becoming slightly askew. These issues are resolved in the multilayer variant. In mean structure diagrams (Fig. 4B), it is evident that the reinforced structure is more stable

and resembles its intended shape. The reinforced area is also consolidated and overlaid with its intended geometry as designed, and the reinforced variant notably aligns better to the input shape (Fig. 4C). Next, reinforcement was applied in two additional cases to study, testing potential weaknesses in narrow and wide geometric features.

The single-layer cone design (Fig. 4D) evaluates the effective range of ring-based design across a range of circumferences. The cone measures only 72 bp in circumference at the tip and 472 bp at the base. Root mean square fluctuations (RMSF) of shapes are calculated from 10^3 snapshots of a 10^8-step trajectory from molecular dynamics simulations and compared to its mean structure calculated across the same snapshots. Visualization of these data shows not only high RMSF at the base but also at the tip of the structure. Narrow rings of curved nanostructures likely form poorly because of being highly strained due to the low radius of curvature while also having little room to add additional crossovers to stabilize the curvature. The peak almost always cannot be resolved in TEM micrographs. On the other hand, despite high RMSF, the base of the cone appears to form well. Reinforcement was then applied at the top six helices, building a second layer around the peak of the cone (Fig. 4E). Running molecular dynamics simulations again (the single layer is consolidated, and the view of the second layer is hidden here for demonstration only), we observe a marked improvement in the RMSF distribution in the peak of the cone and in the yield experimentally, seeing improvements from 62 to 90.60% of well-formed structures as determined by ImageJ analysis of band intensity after gel purification. Furthermore, the tip of the cone is now visible in TEM micrographs (Fig. 4E and figs. S22 and S23) and in their respective 2D class averages.

Next, we evaluated reinforcement in a mushroom design (Fig. 4F and figs. S24 and S25), which is characterized by a wide but thin aspect ratio. The shape also contains sections that slope rapidly both vertically (the stem) and horizontally (the cap). In TEM micrographs, we frequently observed stems forming without caps. In
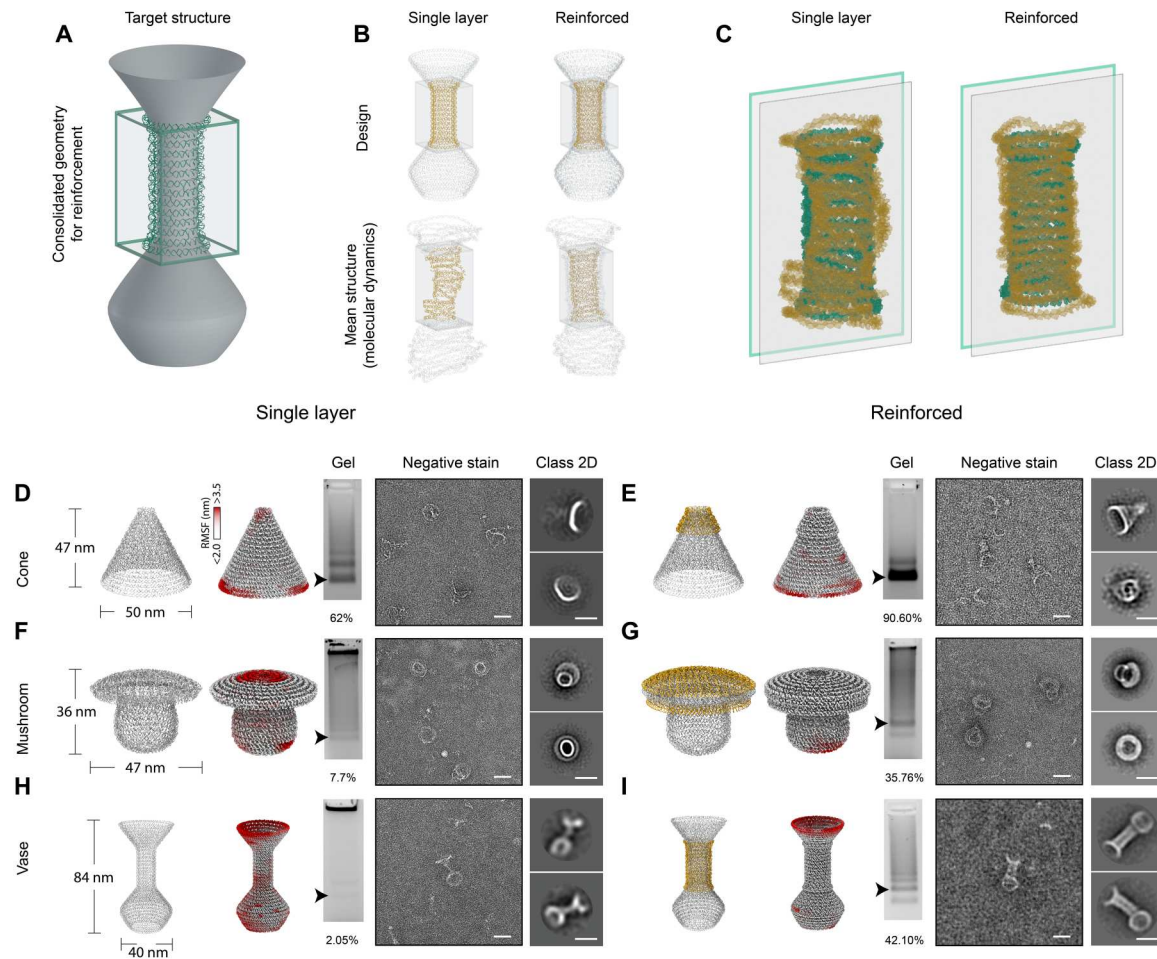
Fig. 4. Characterization of reinforcement strategies. (**A**) A portion of the vase is selected for targeted reinforcement via additional of coplanar helices. (**B**) Designs generated from DNAxiS (top) are submitted into oxDNA (bottom), whereupon mean structures are calculated from 10^3 samples taken uniformly from 10^8 trajectory steps. (**C**) The interior layer (yellow), which determines the shape of the cavity, for both the single layer and reinforced section is consolidated and compared to their intended shape (green). The overlay shows that the reinforced structure more closely conforms to the intended shape of the neck. (**D** to **I**) Comparing additional geometries (gray) using RMSF calculations calculated from trajectory steps generated by oxDNA, yields and shown by AGE, TEM micrographs, and 2D class averages. Scale bars, 40 nm.

RMSF-illustrated diagrams, we notice that, in horizontal sections, as the circumferences of the helices become smaller toward the center of the cap, RMSF rapidly increases. Here, we demonstrate a disjointed application of targeted reinforcement and show that any reinforcing layer can be added tangent to its single-layer profile. Helices for an additional layer are added at the top, along the cap of the mushroom, then skipping the rim (anatomically termed margin), and continuing along the underside of the cap (Fig. 4G). Again, we observe a marked decrease in RMSF as shown in simulations and a significant increase in the yields of fully formed structures (from 7.7 to 35.76% by AGE). The TEM micrographs and their respective 2D class averages also showed that the cap of the mushroom was more resolvable than its nonreinforced counterpart.

Last, we experimentally characterized the vase design (Fig. 4H and figs. S26 and S27) to verify our in silico observations. In the single-layer variant, we frequently observe a neck portion that is poorly formed and often appears as if the cup of the vase becomes separated at the neck from the bulb. When reinforcing the neck (Fig. 4I), structures appear straighter, and most are fully formed with the cup attached. We note that, while the rim of the cup and the midsection of the bulb are similarly wide rings, RMSF is significantly higher along the rim while hardly present in the bulb, and this is most likely due to the structure becoming open-ended at the rim, while the bulb is supported by neighboring helices on both sides. Yields increased markedly from a very low 2.05% up to 42.10%, which possibly shows that there can be specific areas of weakness in some geometries that are more significant toward the formation of the structure. TEM micrographs and their respective 2D class averages showed a clear trend in the stability of the structures, wherein the bulb, stem, and cup regions of the vase were fully resolvable compared to their nonreinforced counterparts.

Design and characterization of asymmetric structures

Fundamentally, the automation provided by DNAxiS is a general strategy for designing DNA origami shapes that exhibit continuous curvature in 3D. Building upon crossover network algorithms initially applied to templates for axially symmetric structures, it was possible to also design several structures with some amount of axial asymmetry to demonstrate the benefits of this rapid automated

approach toward crossover placement (unfortunately, an interface does not yet exist for this in DNAxiS as of this writing). DNAxiS abstracts low-level design of crossovers into quantifiable values. Whereas rings were defined by their circumference, rings could further be consolidated into segments of arcs each defined by their arc length, radius of curvature, and position. Each arc is a module that can be added to the design space and connected to other modules by allowing staple and scaffold strands to run continuously through their end points. Arcs are designed as angled DNA helix bundle upon a square lattice using an insertion-deletion gradient, as in previous work (3), but calculating gradients using a simple Euler-Bernoulli beam model (fig. S28).

Two basic archetypal structures were designed to demonstrate convex and concave geometries. Each structure was designed using varying bundle dimensions [4-helix bundle (two-by-two) up to a 12-helix bundle (four-by-three)] depending on the length of available scaffold and desired rigidity. The ellipse (four-by-three square lattice bundle) was constructed using two each of two arcs (30° and 150°) defined with different inputs of their radius of curvature and arc length (Fig. 5A and figs. S29 and S30). The clover shape merged convex and concave geometries and was constructed with four 180° arcs for the convex leaf sections and four 90° arcs as concave inside corners (Fig. 5B and figs. S31 and S32).

Using the ellipse, we chose to further demonstrate the capabilities of generalized routing by extruding the shape with pitch. Each ellipse was reduced to a two by two bundle and then placed with a 20° rotational offset to its preceding ellipse in the design space, and then the routing algorithms of DNAxiS were applied. Notably, the pitch of the shape eliminates many potential crossover positions, and we allowed DNAxiS to find and apply both parallel and non-parallel crossovers. Upon inclusion of parallel crossovers, the pitched ellipse could finally create enough crossovers to form and appear under TEM imaging (Fig. 5C and figs. S33 and S34).

The clover (three-by-two square lattice bundle) unveils a problem that is most likely unique to DNA nanostructures that have inflection points within a continuous, curved perimeter, which has rarely appeared in prior works. Defining each module of the clover naively according to the angles as they appear often caused the synthesized structure to "round out" as seen in Fig. 5B and fig. S32. We suggest that at module boundaries, where there is an inflection between concave and convex geometry, a mismatch of stresses can cause the structure to misform. A higher-strained module (in this case, the convex leaf section) could overwhelm an adjacent module (in this case, the concave inside corners) as an effect of dissipating strain from its own area. To strengthen the concave sections, an "overcompensation" strategy was proposed to increase the strain of inside corner modules in a direction opposite to the strain produced by the leaf modules.

We used the rapid prototyping capabilities of DNAxiS to test this possibility by iteratively designing and simulating a range of angles for the inside corner of the clover. Furthermore, the bundle cross section was scaled up to a three-by-three square lattice to increase the achievable stiffness of the inside corner. In 10° increments, prospective designs were filtered by adding oxDNA simulations into the design pipeline. As the internal angle of the concave section increased from 90° to 140°, we observed minimal gain past 140°, and the shape conformation of the sample as viewed in TEM also became closer to the intended geometry. Under TEM micrographs and 2D class averages, we observed a similar change in the

synthesized shape, which verified our overcompensation strategy (Fig. 5D and figs. S35 and S36).

DISCUSSION

DNAxiS is uniquely the first software tool to apply automated routing techniques based on heuristic optimization algorithms. As DNA nanostructures increase in scale, with less regularity and more independently designed components, designs may move into a space that becomes intractable for human designers while also lacking sufficient algorithmic regularity. Our work presents an approach for novel DNA origami designs as oblique, freeform structures, which may enable the design of novel geometries, thus enabling wider accessibility to the field for the larger scientific community. We demonstrated how this strategy can succeed for curved DNA origami designs, forming enclosed shapes that do not have any apparent algorithmic regularity to exploit. We described the design complexity that arises from structures that have nonhomogeneous helical twist, notably of which is skewing the periodicity of crossover positions to a point where it becomes tedious for a human designer to arrange a stable crossover network. Having to repeat this for each unique crossover pattern between adjacent helices can quickly become overwhelming for a human designer and can become a barrier for applying DNA nanotechnologies across interdisciplinary applications. This work introduced design principles that include multilayer design of curved and enclosed shapes and characterized the effect of reinforcement on the yield and shape accuracy of structures. Furthermore, the benefits of automation and software modeling were demonstrated in axially asymmetric shapes that took advantage of the ability to rapidly edit geometries and calculate crossover networks. These functionalities can continue to be developed for the future to investigate and generalize methods for DNA origami design for optimization and shape complexity (figs. S37 to S39). A potential impact of our work is to motivate wider consideration of the design and manipulation of globular and more biomimetic DNA nanostructure.

MATERIALS AND METHODS
Inputs
Bowl, gourd, sphere, cone, mushroom, ellipse, and clover shapes were designed with the initial algorithm using fixed crossover counts and crossover alignments up to 3.5. Vase shapes were generated using the simulated annealing algorithm with variable crossover counts and a consistent crossover alignment of 3.0. All helix circumferences were rounded to a crossover factor of 4. Refer to data S1 for specific helical geometries of each design and data S2 for sequence outputs.

Reagents
Staple strands (unpurified) of DNA origami were purchased from Integrated DNA Technologies and were used without any further purification. High-purity scaffolds (p7249 and p8064) were obtained from Tilibit Nanosystems (Germany). PhiX virion singlestranded DNA scaffold was obtained from New England Biolabs.

Formation of DNA origami structures
The details of folding condition and structural components (scaffold, staples, and buffer concentration) are listed in table S2. The
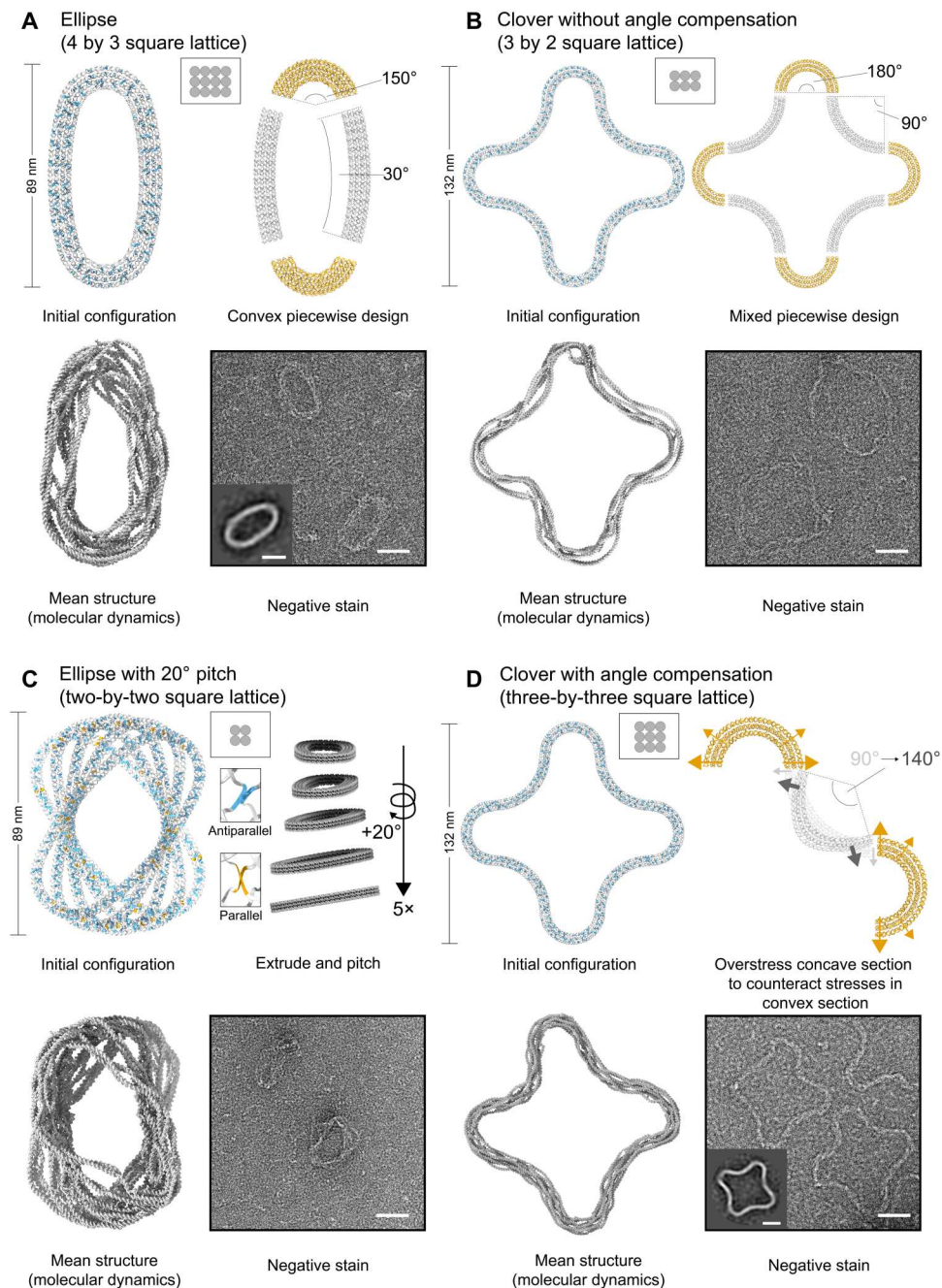
Fig. 5. Exploration of axially asymmetric structures and generalized application of DNAxiS design principles. (**A** and **B**) Modules defined as arcs can be linked together to create axially asymmetric shapes. Each module is a bent bundle of variable cross-sectional helices where design principles implemented in DNAxiS for multilayer structures can directly apply and were used to generate ellipse and clover shapes. (**C**) The ellipse shape is repeated five times in a vertical extrusion and pitched by 20°. The cross-sectional area of each ellipse is reduced to fit the entire design within a limited length of scaffold sequence despite already using multiple scaffolds. Both parallel and antiparallel crossovers are created to increase the crossover count and yield of the design. (**D**) The cross section of bundles is expanded to three by three to increase the upper-bounded stiffness of each module. This is necessary to achieve sufficient counteracting strain on inside corner modules to preserve the inflection between convex to concave segments of the structure without "rounding out" as it did in three-by-two clover. Scale bars (on TEM micrographs and 2D averages), 40 nm.

folding mixtures were prepared in in-house–prepared 1× TAE-Mg^{2+} buffer [20 mM tris base, 10 mM acetic acid, 0.5 mM EDTA, and 12.5 to 20 mM Mg(OAc)$_2$ (pH 8)]. The reaction mixtures were folded in a thermocycler (Life Technologies SimpliAmp).

Twelve-hour annealing protocol
The reaction mixtures were heated to 90°C for 5 min, jump to 86°C for 5 min, and then decrease by 1°C/5 min until 71°C; 70°C for 15 min and decrease by 1°C/15 min to 40°C; 39°C for 10 min and decrease by 1°C/10 min to 26°C; and 25°C for 30 min, jump to 20°C for 15 min, jump to 15°C for 5 min, and jump to 10°C and maintained at that temperature.

Twenty-four-hour annealing protocol
The reaction mixtures were heated to 90°C for 5 min, jump to 86°C for 5 min, and then decrease by 1°C/5 min until 76°C; 75°C for 15 min and decrease by 1°C/15 min until 71°C; 70°C for 20 min and decrease by 1°C/20 min to 61°C; 60°C for 30 min and decrease by 1°C/30 min until 30°C; 29°C for 20 min and decrease by 1°C/20 min to 25°C; 24°C for 15 min and decrease by 1°C/15 min to 20°C; and 19°C for 10 min, decrease by 1°C/10 min to 15°C, jump to 4°C, and pause maintained at that temperature.

Thirty-seven-hour annealing protocol
The reaction mixtures were heated to 80°C for 4 min and then decrease by 1°C/4 min until 61°C; 60.5°C for 30 min and decrease by 0.5°C/30 min until 34.5°C; and 34°C for 60 min and decrease by 1°C/60 min to 24°C, and then pause maintained at that temperature.

Forty-eight-hour annealing protocol
The reaction mixtures were heated to 90°C for 5 min, jump to 86°C for 5 min, and then decrease by 1°C5 min until 81°C; 80°C for 10 min and decrease by 1°C/10 min until 75°C; 74°C for 30 min and decrease by 1°C/30 min to 69°C; 68°C for 40 min and decrease by 1°C/40 min until 53°C; 52°C for 60 min and decrease by 1°C/60 min to 25°C; 24°C for 80 min and decrease by 1°C/80 min to 21°C; and 20°C for 30 min, 19°C for 10 min, decrease by 1°C/10 min to 15°C, jump to 4°C, and pause maintained at that temperature.

Gel electrophoresis of the DNA origami structures
Characterization of folded structures
Samples were run on a prestained 1.2% agarose gel (with ethidium bromide) made in 1× TAE–12.5 mM MgCl$_2$ buffer. The running buffer was 1× TAE–12.5 mM MgCl$_2$. Ten microliters of the annealed sample from the polymerase chain reaction, along with 1 μl of 10× loading dye, was run in each of the wells of the agarose gel. The gels were run for 1 to 1.5 hours at a constant voltage of 80 V at 4°C.

Purification of the folded structures
The fully annealed samples were run on a prestained 1.2% agarose gel (with ethidium bromide) with 20 μl (18 μl of sample and 2 μl of loading dye) being loaded into each well and ran for 90 min at a constant voltage of 80 V at 4°C. The running buffer was 1× TAE–12.5 mM MgCl$_2$. Thereafter, the second lowest band, in some casesthe band above that, was cut out separately, which was put into a Freeze 'N Squeeze tube (the lowest band is the excess staples, so they were left out). Care was taken not to further chop up the bands cut out, which if done, was realized to reduce the yield of the fully formed structures; thus, the rationale was to load them into smaller wells and take the bands out as they appeared. The Freeze 'N Squeeze tubes were left in the −20°C freezer for over 1 to 2 hours (longer periods did not affect the recovery yield of the structures). Afterward, the frozen tubes were spun down at 1600 relative

centrifugal force (rcf) in a tabletop centrifuge for 45 to 50 min at room temperature (lower centrifugation speeds ensures that the assembled structures do not fall apart, and the longer times ensure maximum recovery from the gel pieces). The recovered solution was concentrated using 100-kDa Amicon filters (prerun with filtered 1× TAE–12.5 mM MgCl$_2$ to make the membranes compatible) and spun at 1600 rcf using a tabletop centrifuge.

Negative-stain TEM and image processing
Negative-stain TEM sample preparation
The above purified sample (5 μl) was adsorbed on a commercially supplied formvar-stabilized carbon type-B, 400-mesh copper grids (Ted Pella, part number 01814-F) that was glow-discharged for 1 min at 15 mA using a Pelco easiGlow glow-discharge system (Ted Pella, Redding, CA, USA) and stained using 5 μl of a freshly prepared 2% aqueous uranyl formate solution containing 25 mM NaOH. Samples were incubated for 15 to 300 s depending on the concentration of the sample. Excess liquid was wicked away with Whatmann filter paper, and grids were left to dry for 30 to 60 min before imaging.

Images were acquired on an FEI Tecnai TF20 TEM microscope operated at 120 kV of accelerating voltage using a charge-coupled device camera at ×50,000 magnification. Particles (see details in table S3) were manually picked and class-averaged using Relion3.0 without CTF correction.

Cryo–electron microscopy
Cryo–electron microscopy sample preparation
DNA nanostructures were formed and purified as above. The sample assembly was confirmed and further purified on agarose gels. To remove excess ethidium bromide in the sample buffer, the sample was dialyzed using a 10-kDa Float-A-Lyzer against 1× TAE–12.5 mM MgCl$_2$ and then concentrated as before.

Structured DNA complexes were absorbed to a glow-discharged ultrathin carbon film, supported by a lacey carbon film on a 400-mesh grid (Protochips, Morrisville NC) for 1 min with eight repeated applications. Samples were applied to only one side of the carbon support with precaution to ensure that the grids were left a little wet between applications. Grids were directly plunged frozen into an ethane slurry at liquid nitrogen temperatures. Tilt series images of the samples were collected on a Titan Krios G2 (FEI/Thermo Fisher Scientific) and K2 summit (Gatan, Pleasanton, CA) camera at ×28,735 magnification from −65° to +65° α with a 2° increment between images using batch methods in serial electron microscopy, with a dose-symmetric tomography scheme (61, 62). The IMOD package (63) was used to reconstruct tomograms and visualize tilt series to determine the structures.

Individual particle videos
All images were collected at 14,000× on the microscope at 300 keV with a 1.74 Å per pixel sampling rate in counting mode on a K2 summit direct electron detector. During tomographic reconstruction, images were down-sampled to improve contrast to 7 Å per pixel. Scale bars are17.5 nm.

Supplementary Materials
This PDF file includes:
Supplementary Materials and Methods

Figs. S1 to S39
Tables S1 to S3

Other Supplementary Material for this manuscript includes the following:
Movies S1 to S14
Data S1 to S3

REFERENCES AND NOTES

1. P. W. K. Rothemund, Folding DNA to create nanoscale shapes and patterns. *Nature* **440**, 297–302 (2006).

2. S. M. Douglas, H. Dietz, T. Liedl, B. Högberg, F. Graf, W. M. Shih, Self-assembly of DNA into nanoscale three-dimensional shapes. *Nature* **459**, 414–418 (2009).

3. H. Dietz, S. M. Douglas, W. M. Shih, Folding DNA into twisted and curved nanoscale shapes. *Science* **325**, 725–730 (2009).

4. D. Han, S. Pal, J. Nangreave, Z. Deng, Y. Liu, H. Yan, DNA origami with complex curvatures in three-dimensional space. *Science* **332**, 342–346 (2011).

5. F. Zhang, S. Jiang, S. Wu, Y. Li, C. Mao, Y. Liu, H. Yan, Complex wireframe DNA origami nanostructures with multi-arm junction vertices. *Nat. Nanotechnol.* **10**, 779–784 (2015).

6. R. Veneziano, S. Ratanalert, K. Zhang, F. Zhang, H. Yan, W. Chiu, M. Bathe, Designer nanoscale DNA assemblies programmed from the top down. *Science* **352**, 1534–1534 (2016).

7. E. Benson, A. Mohammed, J. Gardell, S. Masich, E. Czeizler, P. Orponen, B. Högberg, DNA rendering of polyhedral meshes at the nanoscale. *Nature* **523**, 441–444 (2015).

8. R. Iinuma, Y. Ke, R. Jungmann, T. Schlichthaerle, J. B. Woehrstein, P. Yin, Polyhedra self-assembled from DNA tripods and characterized with 3D DNA-PAINT. *Science* **344**, 65–69 (2014).

9. Y. Zhou, J. Dong, C. Zhou, Q. Wang, Finite assembly of three dimensional DNA hierarchical nanoarchitectures through orthogonal and directional bonding. *Angew. Chem.* **134**, e202116416 (2022).

10. G. Yao, F. Zhang, F. Wang, T. Peng, H. Liu, E. Poppleton, P. Šulc, S. Jiang, L. Liu, C. Gong, X. Jing, X. Liu, L. Wang, Y. Liu, C. Fan, H. Yan, Meta-DNA structures. *Nat. Chem.* **12**, 1067–1075 (2020).

11. H. Chandran, N. Gopalkrishnan, B. Yurke, J. Reif, Meta-DNA: A DNA-based approach to synthetic biology, in *A Systems Theoretic Approach to Systems and Synthetic Biology II: Analysis and Design of Cellular Systems*, V. V. Kulkarni, G.-B. Stan, K. Raman, Eds. (Springer, 2014), pp. 171–200.

12. G. Tikhomirov, P. Petersen, L. Qian, Fractal assembly of micrometre-scale DNA origami arrays with arbitrary patterns. *Nature* **552**, 67–71 (2017).

13. K. F. Wagenbauer, C. Sigl, H. Dietz, Gigadalton-scale shape-programmable DNA assemblies. *Nature* **552**, 78–83 (2017).

14. T. Gerling, K. F. Wagenbauer, A. M. Neuner, H. Dietz, Dynamic DNA devices and assemblies formed by shape-complementary, non–base pairing 3D components. *Science* **347**, 1446–1452 (2015).

15. C. Sigl, E. M. Willner, W. Engelen, J. A. Kretzmann, K. Sachenbacher, A. Liedl, F. Kolbe, F. Wilsch, S. A. Aghvami, U. Protzer, M. F. Hagan, S. Fraden, H. Dietz, Programmable icosahedral shell system for virus trapping. *Nat. Mater.* **20**, 1281–1289 (2021).

16. L. Shani, A. N. Michelson, B. Minevich, Y. Fleger, M. Stern, A. Shaulov, Y. Yeshurun, O. Gang, DNA-assembled superconducting 3D nanoscale architectures. *Nat. Commun.* **11**, 5697 (2020).

17. W. Liu, M. Tagawa, H. L. Xin, T. Wang, H. Emamy, H. Li, K. G. Yager, F. W. Starr, A. V. Tkachenko, O. Gang, Diamond family of nanoparticle superlattices. *Science* **351**, 582–586 (2016).

18. Q. Shen, T. Tian, Q. Xiong, P. D. Ellis Fisher, Y. Xiong, T. J. Melia, C. P. Lusk, C. Lin, DNA-origami nanotrap for studying the selective barriers formed by phenylalanine-glycine-rich nucleoporins. *J. Am. Chem. Soc.* **143**, 12294–12303 (2021).

19. K. Zhou, Y. Ke, Q. Wang, Selective in situ assembly of viral protein onto DNA origami. *J. Am. Chem. Soc.* **140**, 8074–8077 (2018).

20. K. Zhou, Y. Zhou, V. Pan, Q. Wang, Y. Ke, Programming dynamic assembly of viral proteins with DNA origami. *J. Am. Chem. Soc.* **142**, 5929–5932 (2020).

21. A. Aghebat Rafat, S. Sagredo, M. Thalhammer, F. C. Simmel, Barcoded DNA origami structures for multiplexed optimization and enrichment of DNA-based protein-binding cavities. *Nat. Chem.* **12**, 852–859 (2020).

22. B. Saccà, R. Meyer, M. Erkelenz, K. Kiko, A. Arndt, H. Schroeder, K. S. Rabe, C. M. Niemeyer, Orthogonal protein decoration of DNA origami. *Angew. Chem.* **122**, 9568–9573 (2010).

23. E. Nakata, F. F. Liew, C. Uwatoko, S. Kiyonaka, Y. Mori, Y. Katsuda, M. Endo, H. Sugiyama, T. Morii, Zinc-finger proteins for site-specific protein positioning on DNA-origami structures. *Angew. Chem. Int. Ed.* **51**, 2421–2424 (2012).

24. P. Kosuri, B. D. Altheimer, M. Dai, P. Yin, X. Zhuang, Rotation tracking of genome-processing enzymes using DNA origami rotors. *Nature* **572**, 136–140 (2019).

25. T. Aksel, Z. Yu, Y. Cheng, S. M. Douglas, Molecular goniometers for single-particle cryo-electron microscopy of DNA-binding proteins. *Nat. Biotechnol.* **39**, 378–386 (2021).

26. C. Close, K. Trofymchuk, L. Grabenhorst, B. Lalkens, V. Glembockyte, P. Tinnefeld, Maximizing the accessibility in DNA origami nanoantenna plasmonic hotspots. *Adv. Mater. Interfaces* **9**, 2200255 (2022).

27. E. Silvester, B. Vollmer, V. Pražák, D. Vasishtan, E. A. Machala, C. Whittle, S. Black, J. Bath, A. J. Turberfield, K. Grünewald, L. A. Baker, DNA origami signposts for identifying proteins on cell membranes by electron cryotomography. *Cell* **184**, 1110–1121.e16 (2021).

28. T. G. Martin, T. A. M. Bharat, A. C. Joerger, X. Bai, F. Praetorius, A. R. Fersht, H. Dietz, S. H. W. Scheres, Design of a molecular support for cryo-EM structure determination. *Proc. Natl. Acad. Sci. U.S.A.* **113**, E7456–E7463 (2016).

29. Z. Zhao, J. Fu, S. Dhakal, A. Johnson-Buck, M. Liu, T. Zhang, N. W. Woodbury, Y. Liu, N. G. Walter, H. Yan, Nanocaged enzymes with enhanced catalytic activity and increased stability against protease digestion. *Nat. Commun.* **7**, 10619 (2016).

30. Y. Zhang, Z. Qu, C. Jiang, Y. Liu, R. Pradeep Narayanan, D. Williams, X. Zuo, L. Wang, H. Yan, H. Liu, Prescribing silver chirality with DNA origami. *J. Am. Chem. Soc.* **143**, 8639–8646 (2021).

31. R. Schreiber, N. Luong, Z. Fan, A. Kuzyk, P. C. Nickels, T. Zhang, D. M. Smith, B. Yurke, W. Kuang, A. O. Govorov, T. Liedl, Chiral plasmonic DNA nanostructures with switchable circular dichroism. *Nat. Commun.* **4**, 2948 (2013).

32. H. Jun, T. R. Shepherd, K. Zhang, W. P. Bricker, S. Li, W. Chiu, M. Bathe, Automated sequence design of 3D polyhedral wireframe DNA origami with honeycomb edges. *ACS Nano* **13**,2, 2083–2093 (2019).

33. Y. Ke, S. M. Douglas, M. Liu, J. Sharma, A. Cheng, A. Leung, Y. Liu, W. M. Shih, H. Yan, Multilayer DNA origami packed on a square lattice. *J. Am. Chem. Soc.* **131**, 15903–15908 (2009).

34. Y. Ke, N. V. Voigt, K. V. Gothelf, W. M. Shih, Multilayer DNA origami packed on hexagonal and hybrid lattices. *J. Am. Chem. Soc.* **134**, 1770–1774 (2012).

35. T. G. Martin, H. Dietz, Magnesium-free self-assembly of multi-layer DNA objects. *Nat. Commun.* **3**, 1103 (2012).

36. Y. Ke, G. Bellot, N. V. Voigt, E. Fradkov, W. M. Shih, Two design strategies for enhancement of multilayer–DNA-origami folding: Underwinding for specific intercalator rescue and staple-break positioning. *Chem. Sci.* **3**, 2587–2597 (2012).

37. S. Helmi, C. Ziegler, D. J. Kauert, R. Seidel, Shape-controlled synthesis of gold nanostructures using DNA origami molds. *Nano Lett.* **14**, 6693–6698 (2014).

38. W. Sun, E. Boulais, Y. Hakobyan, W. L. Wang, A. Guan, M. Bathe, P. Yin, Casting inorganic structures with DNA molds. *Science* **346**, 1258361 (2014).

39. G. Grossi, M. D. E. Jepsen, J. Kjems, E. S. Andersen, Control of enzyme reactions by a reconfigurable DNA nanovault. *Nat. Commun.* **8**, 992 (2017).

40. V. Linko, M. Eerikäinen, M. A. Kostiainen, A modular DNA origami-based enzyme cascade nanoreactor. *Chem. Commun.* **51**, 5351–5354 (2015).

41. S. F. J. Wickham, A. Auer, J. Min, N. Ponnuswamy, J. B. Woehrstein, F. Schueder, M. T. Strauss, J. Schnitzbauer, B. Nathwani, Z. Zhao, S. D. Perrault, J. Hahn, S. Lee, M. M. Bastings, S. W. Helmig, A. L. Kodal, P. Yin, R. Jungmann, W. M. Shih, Complex multicomponent patterns rendered on a 3D DNA-barrel pegboard. *Nat. Commun.* **11**, 5768 (2020).

42. Y. Yang, J. Wang, H. Shigematsu, W. Xu, W. M. Shih, J. E. Rothman, C. Lin, Self-assembly of size-controlled liposomes on DNA nanotemplates. *Nat. Chem.* **8**, 476–483 (2016).

43. Z. Zhang, Y. Yang, F. Pincet, M. C. Llaguno, C. Lin, Placing and shaping liposomes with reconfigurable DNA nanocages. *Nat. Chem.* **9**, 653–659 (2017).

44. M. Langecker, V. Arnaut, T. G. Martin, J. List, S. Renner, M. Mayer, H. Dietz, F. C. Simmel, Synthetic lipid membrane channels formed by designed DNA nanostructures. *Science* **338**, 932–936 (2012).

45. S. Dey, A. Dorey, L. Abraham, Y. Xing, I. Zhang, F. Zhang, S. Howorka, H. Yan, A reversibly gated protein-transporting membrane channel made of DNA. *Nat. Commun.* **13**, 2271 (2022).

46. P. M. Arnott, S. Howorka, A temperature-gated nanovalve self-assembled from DNA to control molecular transport across membranes. *ACS Nano* **13**, 3334–3340 (2019).

47. R. P. Thomsen, M. G. Malle, A. H. Okholm, S. Krishnan, S. S.-R. Bohr, R. S. Sørensen, O. Ries, S. Vogel, F. C. Simmel, N. S. Hatzakis, J. Kjems, A large size-selective DNA nanopore with sensing applications. *Nat. Commun.* **10**, 5655 (2019).

48. B. Shen, P. Piskunen, S. Nummelin, Q. Liu, M. A. Kostiainen, V. Linko, Advanced DNA nanopore technologies. *ACS Appl. Bio Mater.* **3**, 5606–5619 (2020).

49. Q. Zhang, Q. Jiang, N. Li, L. Dai, Q. Liu, L. Song, J. Wang, Y. Li, J. Tian, B. Ding, Y. Du, DNA origami as an in vivo drug delivery vehicle for cancer therapy. *ACS Nano* **8**, 6633–6643 (2014).

50. S. M. Douglas, I. Bachelet, G. M. Church, A logic-gated nanorobot for targeted transport of molecular payloads. *Science* **335**, 831–834 (2012).

51. S. Li, Q. Jiang, S. Liu, Y. Zhang, Y. Tian, C. Song, J. Wang, Y. Zou, G. J. Anderson, J.-Y. Han, Y. Chang, Y. Liu, C. Zhang, L. Chen, G. Zhou, G. Nie, H. Yan, B. Ding, Y. Zhao, A DNA nanorobot functions as a cancer therapeutic in response to a molecular trigger in vivo. *Nat. Biotechnol.* **36**, 258–264 (2018).

52. R. E. Kohman, X. Han, Light sensitization of DNA nanostructures via incorporation of photo-cleavable spacers. *Chem. Commun.* **51**, 5747–5750 (2015).

53. Q. Hu, H. Li, L. Wang, H. Gu, C. Fan, DNA nanotechnology-enabled drug delivery systems. *Chem. Rev.* **119**, 6459–6506 (2019).

54. S. Williams, K. Lund, C. Lin, P. Wonka, S. Lindsay, H. Yan, Tiamat: A three-dimensional editing tool for complex DNA structures, in *International Workshop on DNA-Based Computers*, A. Goel, F. C. Simmel, P. Sosík, Eds. (Springer, 2008), pp. 90–101.

55. S. M. Douglas, A. H. Marblestone, S. Teerapittayanon, A. Vazquez, G. M. Church, W. M. Shih, Rapid prototyping of 3D DNA-origami shapes with caDNAno. *Nucleic Acids Res.* **37**, 5001–5006 (2009).

56. C.-M. Huang, A. Kucinic, J. A. Johnson, H.-J. Su, C. E. Castro, Integrated computer-aided engineering and design for DNA assemblies. *Nat. Mater.* **20**, 1264–1271 (2021).

57. L. Rovigatti, P. Šulc, I. Z. Reguly, F. Romano, A comparison between parallelization approaches in molecular dynamics simulations on GPUs. *J. Comput. Chem.* **36**, 1–8 (2015).

58. B. E. K. Snodin, F. Randisi, M. Mosayebi, P. Šulc, J. S. Schreck, F. Romano, T. E. Ouldridge, R. Tsukanov, E. Nir, A. A. Louis, J. P. K. Doye, Introducing improved structural properties and salt dependence into a coarse-grained model of DNA. *J. Chem. Phys.* **142**, 234901 (2015).

59. E. Poppleton, J. Bohlin, M. Matthies, S. Sharma, F. Zhang, P. Šulc, Design, optimization and analysis of large DNA and RNA nanostructures through interactive visualization, editing and molecular simulation. *Nucleic Acids Res.* **48**, e72–e72 (2020).

60. J. Bohlin, M. Matthies, E. Poppleton, J. Procyk, A. Mallya, H. Yan, P. Šulc, Design and simulation of DNA, RNA and hybrid protein–nucleic acid nanostructures with oxView. *Nat. Protoc.* **17**, 1762–1788 (2022).

61. W. J. Hagen, W. Wan, J. A. Briggs, Implementation of a cryo-electron tomography tilt-scheme optimized for high resolution subtomogram averaging. *J. Struct. Biol.* **197**, 191–198 (2017).

62. D. N. Mastronarde, Automated electron microscope tomography using robust prediction of specimen movements. *J. Struct. Biol.* **152**, 36–51 (2005).

63. J. R. Kremer, D. N. Mastronarde, J. R. McIntosh, Computer visualization of three-dimensional image data using IMOD. *J. Struct. Biol.* **116**, 71–76 (1996).